# Correlation between efficiency and device characterization in MAPbI$_{3-x}$Cl$_x$ standard perovskite solar cells

Hanadi Mehdi[1,2] · Muriel Matheron[2] · Asya Mhamdi[1] · Matthieu Manceau[2] · Carine Roux[2] · Solenn Berson[2] · Stéphane Cros[2] · Abdelaziz Bouazizi[1]

## Abstract

Hybrid organic–inorganic halide perovskite solar cells (PSCs) have gained exceptional attention in photovoltaic fields with an attractive yield of 25%. Characterization tools present as an important means that would help define optimized treatment parameters at an early stage of device manufacturing, instead of measuring the $J(V)$ curves of complete solar cells. In this work, devices with planar NIP architecture ITO/SnO$_2$/MAPbI$_{3-x}$Cl$_x$/HTL/Au were elaborated using one-step deposition method. The effects of annealing temperature of the ETL layer (SnO$_2$) and various materials as an HTL layer have been studied. In parallel, X-ray diffraction, UV–visible absorption and photoluminescence were performed as well as photoluminescence spectroscopy, to analyze the active layer crystallinity, absorption properties and to probe charge transfer between perovskite and interface layers. By varying processing parameters, device efficiency could be raised from 10% up to 13.2%.

## 1 Introduction

Recently, hybrid perovskite solar cells (PSCs) have become one of the most important developments in the field of photovoltaic energy. They have attracted much attention due to their great power conversion efficiency (PCE) which has increased from 3.9 to 25.2% in 10 years [1–6]. Hybrid halide perovskites have become a promising materials in the solar field due to their good advantages including high optical absorption coefficient, long carrier diffusion length, high carrier mobility and tunable band structure [7–13]. The degradation and stability of perovskite solar cells depend on several parameters, among which layers composition plays an important role. It was reported that the incorporation of chloride (Cl–) in the starting materials could trigger perovskite crystallization and stabilize the MAPbI$_3$ lattice [14,

15]. Furthermore, using mixed-halide perovskite as an active layer can be useful to control the bandgap and to increase perovskite resistance to decomposition [16]. Consequently, the conversion efficiencies of photovoltaic devices were improved with MAI and PbCl$_2$ precursors.

Furthermore, many factors can influence the efficiency of the perovskite solar cells. In this circumstance, many efforts have been developed to improve the photovoltaic performance and to enhance the stability of the perovskite cells, as well as the perovskite deposition process [17–19], the annealing treatment [20, 21], the solvent engineering [15, 22], doping of perovskite material [23, 24], the perovskite solar cells structure [20, 25, 26], use of various electron and hole transport materials [27, 28] and doping of transport materials layer deposition processes [29].

Generally, standard perovskite solar cells are manufactured using titanium oxide (or other metallic oxides) as the electron transport layer (ETL) and 2,2′-7,7′-tetrakis (N, N-di-p-methoxyphenylamine)-9.9′-spirobifluorene (spiro-OMeTAD) as a hole transport layer (HTL) [30]. However, titanium oxides require high treatment temperature of titanium oxide and the spiro-OMeTAD suffers from very high cost and low stability. Indeed, this organic HTL material requires a complicated synthesis in several stages and is generally expensive which limits further the development of perovskite solar cells, especially in flexible substrates.

✉ Hanadi Mehdi
hanadi.mehdi92@gmail.com

1 Équipe Dispositifs Électroniques Organiques et Photovoltaïque Moléculaire, Univ Monastir, LMCN, FSM 5019 Monastir, Tunisie

2 Univ. Grenoble Alpes, CEA, LITEN, INES, 73375 Le Bourget-du-Lac, France

As it was cited in the previous paragraph, optimizing the interface layer is an important step in perovskite solar cell efficiency improvement. It was recommended to select interface transport layers with high charge carrier's extraction. Recently, it has been demonstrated that the Tin(IV) oxide "$SnO_2$" appears to be a better ETL for PSCs [31] compared to Titanium oxide (IV)"$TiO_2$" [3] or Zinc oxide "ZnO" [32] due to its high mobility and low trap density.

A detailed study of the annealing treatments of the $SnO_2$ (ETL layer) is demonstrated in this study. Three thermal annealing temperatures are used: 200, 220 and 240 °C. The nature of the HTL layer was also investigated. Two-hole transport materials, P3HT and PTAA, were used.

Different characterization tools were used like the XRD diffraction to study the crystallinity of the materials, the absorption allowing the study of the material absorption capacity, which affects directly the short-circuit current, and the photoluminescence PL to study the mechanism of recombination in the material. A complete device optimization method based on the combination of these different characterizations was used to improve the performance of these devices.

## 2 Experimental section

### 2.1 Materials and solar cell fabrication

ITO-coated glass substrates from Visiontek were cleaned sequentially by a performing ultrasonic treatment in acetone, isopropanol and deionized water for 5 min. A tin (IV) oxide ($SnO_2$) nanoparticle colloidal suspension with a thickness of 25 nm was spin-coated at 4000 rpm for 40 s on cleaned ITO after UV–ozone treatment for 30 min and dried at different heat treatments (200, 220 and 240 °C) for 20 min in air. For the preparation of the perovskite compounds,

methylammonium iodide and lead (II) chloride were dissolved in the glovebox in N. N-dimethylformamide (DMF) at a (3:1)molar ratio, respectively, for (MAI: $PbCl_2$) and then stirred at room temperature overnight in the glove box. After that, a solution of the perovskite was spin-coated on the $SnO_2$ layer at 4000 rpm for 40 s and then annealing at 100 °C for 35 min. A perovskite layer with thickness of 230 nm was obtained. Next, the hole transport layer HTL (P3HT (30 mg/ml), PTAA (10 mg/ml)) was spin-coated at 2000 rpm for 30 s. Finally, to complete the whole solar cells, a thin layer of Au (100 nm) was evaporated on top of the HTL layer. The illustration of the elaborated $CH_3NH_3PbI_{3-x}Cl_x$ hybrid perovskite cell device is shown in Fig. 1.

### 2.2 Materials and device characterization

Perovskite films crystallinity was measured using X-ray diffraction (AerisPANalytical, Benchtop X-ray diffractometer) equipped using CoKα radiation at 40 kV and 15 mA. The UV–Vis spectra were measured by a Hitachi UV-2600 spectrophotometer in the wavelength range of 300 to 900 nm with an integrating sphere. Steady-state photoluminescence spectra were obtained with a 4500-fluorescence spectrometer, with a 450 W monochromatic xenon lamp source and a monochromator (selected wavelength λexc = 500 nm). The amount of charge transfer can be evaluated by calculating the parameter η, which defines the transfer efficiency (quenching efficiency), by using the following known expression [33]:

$$\eta = 1 - I/I_0$$

where $I_0$ and $I$ are, respectively, the integrated PL intensities of the device in the absence and presence of the HTL layer.

The current density–voltage (J–V) curves of solar cells were measured on a Keithley 2402 measure unit under AM1.5 G illumination at 1000 W m$^{-2}$ using an Oriel 9403A-SR1.

Fig. 1 **a** Structure of the device and **b** schematic energy-level diagram
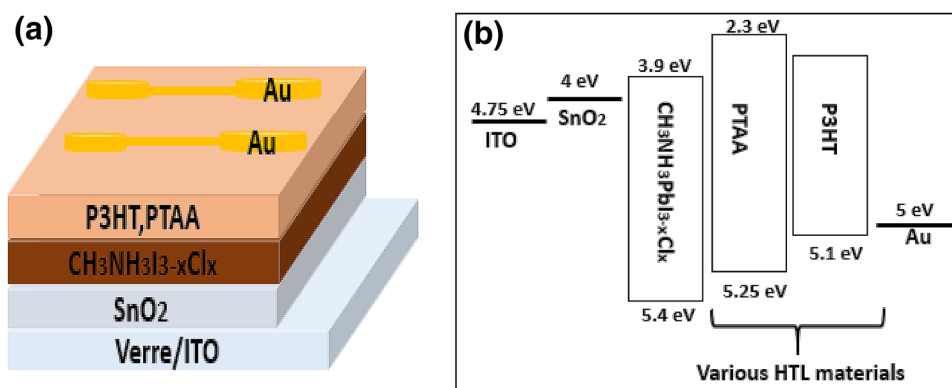
# 3 Results and discussion

Perovskite crystallization is strongly dependent on ETL nature and surface state [34, 35]. Therefore, ETL annealing treatment might affect perovskite crystallinity and device efficiency. In this work, we investigate the annealing effect of the ETL layer ($SnO_2$) on the properties of $MAPbI_{3-x}Cl_x$ films after different annealing temperatures: 200, 220 and 240 °C for 20 min in air.

## 3.1 Effect of annealing temperature of $SnO_2$

### 3.1.1 Crystallinity

The XRD patterns of $MAPbI_{3-x}Cl_x$, ($MA = CH_3NH_3$) on top of the $SnO_2$ layers annealed at different temperatures (200, 220 and 240 °C) are shown in Fig. 2. The XRD patterns of the perovskite layers are approximately the same. Two dominant perovskite peaks appear at 17.11° and 34.03° and are attributed to the (110) and (220) planes, respectively, and another one at 37,85° which corresponds to the (310) planes of tetragonal $MAPbI_3$ [36–38]. We also note the presence of one peak at $2\theta = 18.85°$, corresponding to the (100) plane and attributed to the pure chlorinated perovskite $MAPbCl_3$ [39]. Its presence has already been reported for starting formulations involving MAI and $PbCl_2$ in the same molar ratio (3:1) as ours (refs). In addition, it was noted that the diffraction peak at 12.44° could be attributed to the $PbI_2$ lattice plane.

According to this diffractogram, we can also identify peaks, which are attributed to the ITO, which indicates the passage of the beam through the whole thickness. Since all measurements are made on films with the same thickness, ($SnO_2$ (25 nm) and $MAPbI_{3-x}Clx$ (230 nm)), diffraction peak



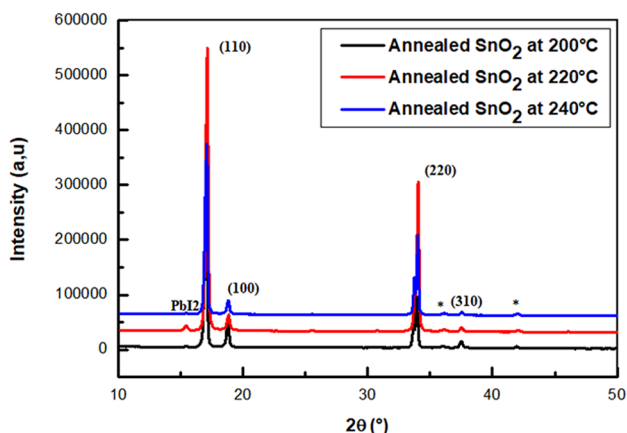**Fig. 2** X-ray diffraction patterns of $MAPbI_{3-x}Cl_x$ films deposited on ITO / $SnO_2$ substrates for different $SnO_2$ annealing temperatures: 200, 220 and 240 °C, (*) peaks attributed to ITO.

intensities could be compared. Or, in a more rigorous way, intensity ratio such as $PbI_2$/MAPI was used for comparison between the different conditions.

As shown in Fig. 2, we can notice that the $SnO_2$/ $MAPbI_{3-x}Cl_x$ film with a layer of $SnO_2$ annealed at 220° C has the highest intensities of the planes (110) and (220).

Furthermore, from the variation of FWHM (full width at half maximum) in the plane (110), extracted from the X-ray diffraction patterns which are illustrated in Table 1, we can notice a low value of FWHM obtained for this same annealing condition (220 °C), suggesting an increase of the crystal sizes [40]. This increase in crystal size can be deduced from the Debye–Scherrer equation [41] and the variations of the perovskite crystal size obtained after different annealing temperatures of $SnO_2$ layer are summarized in Table 1.

$$L = K\lambda/\beta\cos\theta \qquad (1)$$

where $L$ is the average crystallite size, $\lambda$ is the X-ray wavelength in nanometer (nm), $\beta$ is the peak width of the diffraction peak profile at half maximum height resulting from small crystallite size in radians and $K$ is a constant related to crystallite shape, normally taken as 0.9.

Another striking fact pointing at the 220 °C condition is the ratio of $PbI_2$ relative to the amount of MAPI for the different annealing temperatures, with a much larger amount of $PbI_2$ for the 220 °C condition (Fig. 3) with a ratio of 0.006, 0.022 and 0.003 for 200° C, 220° C and 240° C, respectively. The beneficial effect of $PbI_2$ as defect passivation has already been mentioned in the literature [42].

### 3.1.2 Optical band gap and photoluminescence

In order to investigate the annealing effect of the electron transport layer ($SnO_2$) on the optical properties of $MAPbI_{3-x}Cl_x$ films, we have used UV–visible absorption spectra on the perovskite so-called 'half-cells' (glass/ITO/ETL/Perovskite). Figure 4 shows the UV–visible absorption spectra of the $SnO_2$/perovskite films with different annealing temperatures of the ETL layer.

The UV–Vis spectra of all samples show a typical $MAPbI_{3-x}Cl_x$ absorbance, with an onset absorption at 740 nm [13, 34, 43].

**Table 1** Variation of (110) peaks Full Width at Half Maximum (FWHM) and crystal size with the annealing temperature of $SnO_2$

| Annealing temperature of $SnO_2$ (°C) | FWHM (°) | Crystallite size (nm) |
|---|---|---|
| 200 | 0.263 | 354 |
| 220 | 0.220 | 425 |
| 240 | 0.235 | 297 |
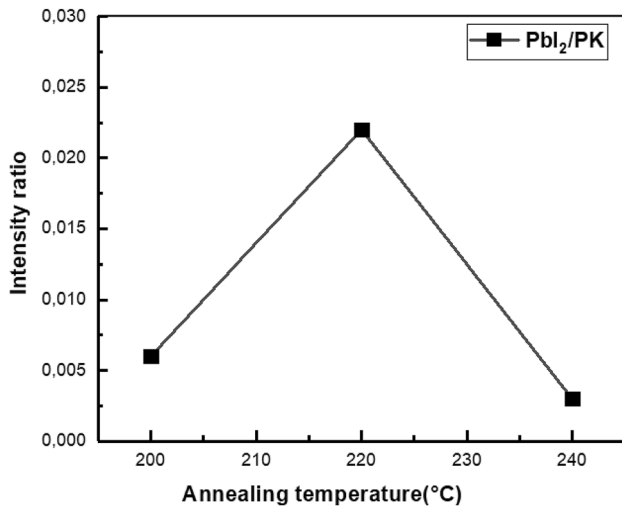
**Fig. 3** Variation of intensity ratios of PbI$_2$/MAPI with the annealing temperature of SnO$_2$



**Fig. 5** Steady-state photoluminescence (PL) spectra of ITO /SnO$_2$/ MAPbI$_{3-x}$Cl$_x$ substrates under different annealing temperatures of SnO2 layer



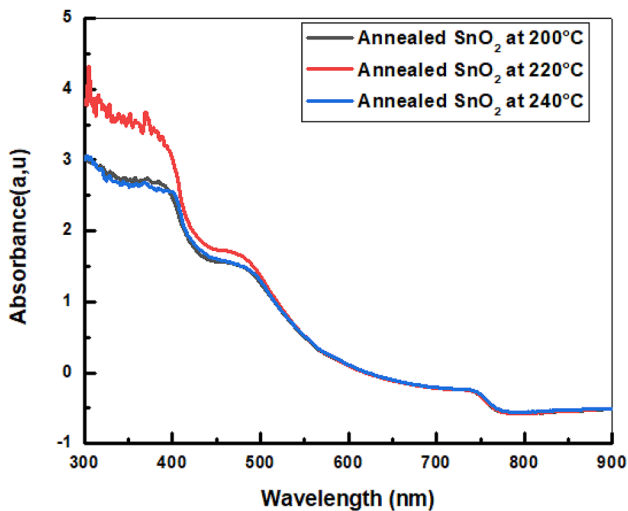**Fig. 4** Absorption spectra of MAPbI$_{3-x}$Cl$_x$ with different annealing temperatures of SnO$_2$ layers (200 °C, 220 °C and 240 °C)

The absorption of the MAPbI$_{3-x}$Cl$_x$ perovskite film at 740 nm peak after various SnO$_2$ layer annealing temperatures was found to be unchanged. Nevertheless, a small additional absorption from 300 to 500 nm was observed for the SnO$_2$ film annealed at 220 °C. This additional absorption may be due to PbI$_2$ which is in accordance with the previous XRD measurement.

Steady-state photoluminescence (PL) spectroscopy was then conducted to evaluate the charge transfer efficiency between perovskite absorber and the SnO$_2$ ETLs. Figure 5 shows the PL spectra of ITO/SnO$_2$/MAPbI$_{3-x}$Cl$_x$ films. In these experiments, all samples exhibit an emission peak at 760 nm (radiative recombination from the valence band to

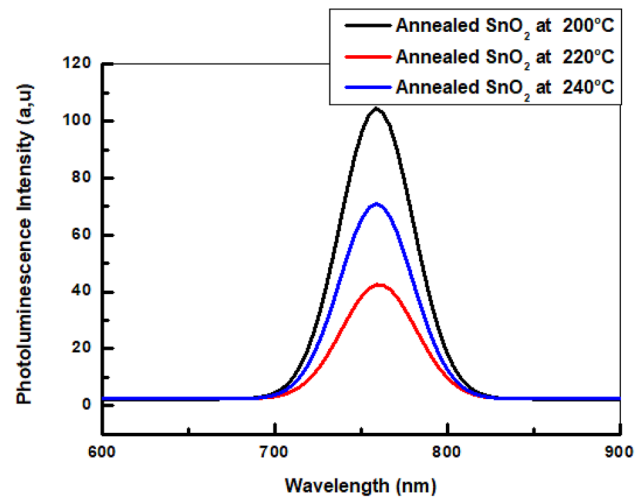conduction band of perovskite), obtained after excitation at 500 nm and originating from MAPbI$_3$ [44].

When looking at the three annealing conditions, it is observed that the variation of the thermal annealing of SnO$_2$ (200, 220 and 240 °C) has induced a change in photoluminescence intensity without a change in the emission peak position. This shows that the gap remains unchanged for the three temperatures. However, a strong quenching of perovskite emission is clearly observed with annealing treatment of the SnO$_2$ layer at 220 °C.

This decrease in the PL intensity indicates the good transfer of charges and the fast transportation of electrons from perovskite films to SnO$_2$ layers [45]. Moreover, this PL quenching efficiency is proof of the high crystallinity of the perovskite film, suggesting an efficient electron transfer from perovskite to the ETL.

### 3.1.3 Photovoltaic performance

Figure 6 shows the photocurrent density–voltage (J–V) characteristics of the best PSCs with the configuration ITO/SnO$_2$/MAPbI$_{3-x}$Cl$_x$ /P3HT/Au, elaborated from different annealing temperatures of SnO$_2$ and measured under AM 1.5 G irradiation (100 mW.cm$^{-2}$). The photovoltaic parameters of the devices are summarized in Table 2. The devices prepared with SnO$_2$ layer and annealed at 220 °C show the highest photovoltaic performance with an open-circuit voltage ($V_{OC}$) of 0.97 V, a short-circuit current ($J_{SC}$) of 20.33 mA/cm$^2$, a fill factor (FF) of 61% and a power conversion efficiency (PCE) of 12.1%. All these parameters are significantly better than those of PSC with SnO$_2$ layer, annealed at 200 °C ($J_{SC}$ =19.41 mA/cm$^2$, $V_{OC}$ =0.89 V,
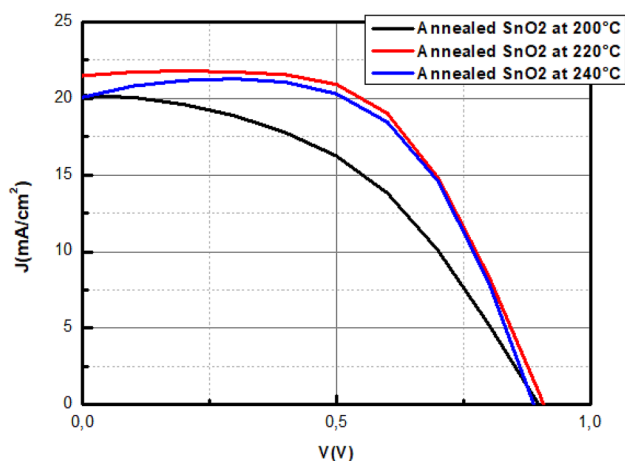
**Fig. 6** *J–V* characteristics of the best PSCs fabricated from different annealing temperatures of $SnO_2$

FF = 55%, PCE = 10.3%) and 240 °C ($J_{SC}$ = 19.45 mA/cm$^2$, $V_{OC}$ = 0.90 V, FF = 62%, PCE = 11.1%).

The device with the $SnO_2$ layer annealed at 200 °C has the worst curve with a low FF. This poor FF is linked to low shunt resistance and high series resistance. The high PL obtained for such condition, indicating the poor charge transfer from perovskite to ETL, which could be linked to this higher series resistance.

The enhancement of the $J_{SC}$ for annealing at 220 °C can be attributed to the slight enhancement of the absorption around 490 nm as observed previously in Fig. 4.

The improvement of FF and $V_{OC}$ at 220 °C could be attributed to the improved quality of the perovskite film and the low electron agglomeration in the $SnO_2$ layer, which greatly reduces the recombination rate. Thus, the annealing temperature of $SnO_2$ at 220 °C appears to be an optimum for the operation of the cells with the highest absorption, which leads to the best $J_{SC}$.

After fixing the optimum annealing temperature of the ETL layer at 220° C, we have moved to study the influence

of the HTL layer on the performance of the perovskite solar cells. A series of $MAPbI_{3-x}Clx$ perovskites solar cells were elaborated with different HTL layers: PTAA and P3HT.

## 3.2 Effect of the nature of HTL

### 3.2.1 Ultraviolet–Visible Absorption

To further investigate the effect of the HTL layer, we performed UV–visible absorption spectroscopy. As shown in Fig. 7, all films show a typical absorbance spectrum of $MAPbI_{3-x}Cl_x$. The absorption spectrum of the P3HT deposited on the ITO/$SnO_2$/ PVK substrate shows an additional absorption, in the zone ranging from 450 to 650 nm, which is due to the absorption of the P3HT material (Fig. 7b [46]).
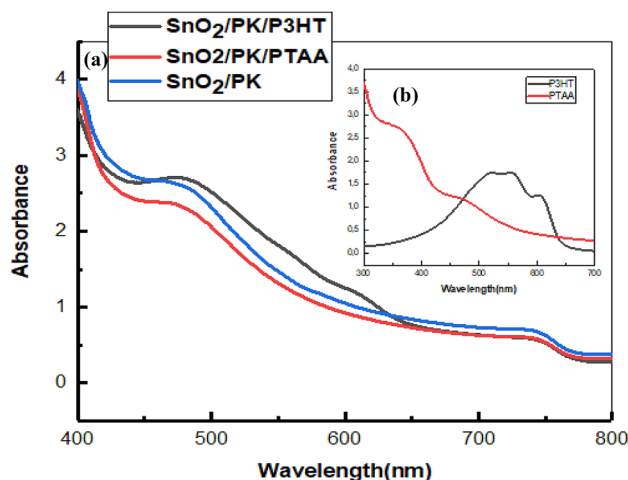


**Fig. 7 a** Absorption spectra of the ITO/$SnO_2$ / $MAPbI_{3-x}Cl_x$/P3HT and ITO/$SnO_2$/$MAPbI_{3-x}Cl_x$/PTAA structures. **b** Absorption spectrum of P3HT and absorption spectrum of PTAA

**Table 2** Photovoltaic parameters extracted from the champion and average solar cells fabricated from different annealing temperatures of $SnO_2$

| Annealing temperature(°C) | | $V_{OC}$ (V) | $J_{SC}$ (mA/cm$^2$) | FF (%) | PCE (%) | $R_S$ (ohm.cm$^2$) | $R_{SC}$ (ohm.cm$^2$) |
|---|---|---|---|---|---|---|---|
| 200 | Best | 0.89 | 19.60 | 55 | 10.3 | 8.39 | 136.09 |
| | Average | 0.99 | 18.82 | 57 | 10.0 | 7.92 | 144.56 |
| | Standard deviation | 2.46 | 0.51 | 0.14 | 0.29 | 0.65 | 10.85 |
| 220 | Best | 0.97 | 20.33 | 61 | 12.1 | 6.66 | 182.04 |
| | Average | 0.96 | 20.58 | 60 | 11.9 | 7.63 | 274.63 |
| | Standard deviation | 7.29 | 0.36 | 1.54 | 0.19 | 1.36 | 130.93 |
| 240 | Best | 0.90 | 19.75 | 62 | 11.1 | 7.24 | 190.57 |
| | Average | 0.91 | 18.63 | 65 | 11.0 | 7.07 | 196.74 |
| | Standard deviation | 8.50 | 1.15 | 2.47 | 0.01 | 196.74 | 8.73 |

### 3.2.2 Photoluminescence

To further elucidate the process of the photo-generated electron–hole separation and injection by using different HTL layers, steady-state photoluminescence spectra were performed and are displayed in Fig. 8, which shows the PL spectra of ITO/SnO$_2$/PK, ITO/SnO$_2$/PVK/P3HT and ITO/SnO$_2$/PVK/PTAA structure.

We note a blue shift for the ITO/SnO$_2$/PVK/P3HT film and the presence of a second peak with a low-intensity emission around 650 nm. The 650 nm contribution is attributed to the P3HT emission because the P3HT can also absorb at 500 nm and it emits between 600 and 800 nm. The blue-shifted emission at 725 nm could be explained by a decrease in the crystallinity of the film that was well confirmed by the measure XRD (Fig. 1 information support).

The sample-based on PTAA shows a higher degree of PL quenching than the P3HT, indicating a good separation efficiency of charge carriers and an increase in the crystallinity [34].

A quenching of perovskite PL emission was observed after the deposition of the HTL layer (P3HT or PTAA), with a quenching efficiency η of 64.84% and 68.90% for the P3HT and PTAA, respectively.

Furthermore, these results are explained by the difference in the energy level of the highest occupied molecular orbital between CH$_3$NH$_3$PbI$_{3-x}$Cl$_x$ and PTAA, which was lower than that with P3HT as shown in Fig. 1. Further, the exciton at the CH$_3$NH$_3$PbI$_{3-x}$Cl$_x$/P3HT interface could be easily recombined that due to the poor electronic conductivity of P3HT, which is a consequence of the higher barrier holes collection of P3HT [34].
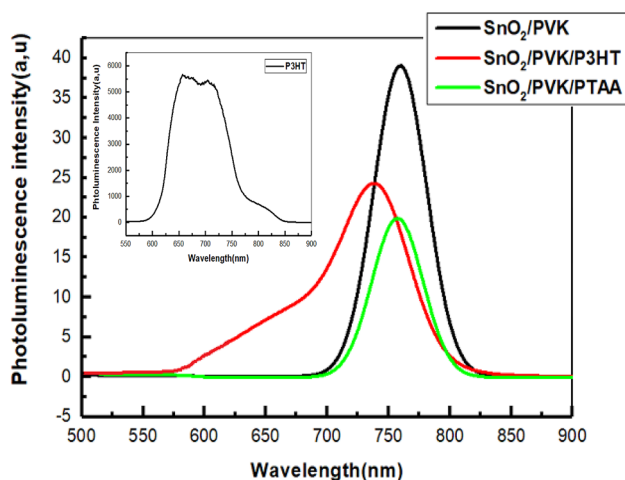


**Fig. 8** Photoluminescence spectra for the two HTL deposited on ITO/SnO$_2$/MAPbI$_{3-x}$Cl$_x$ substrate
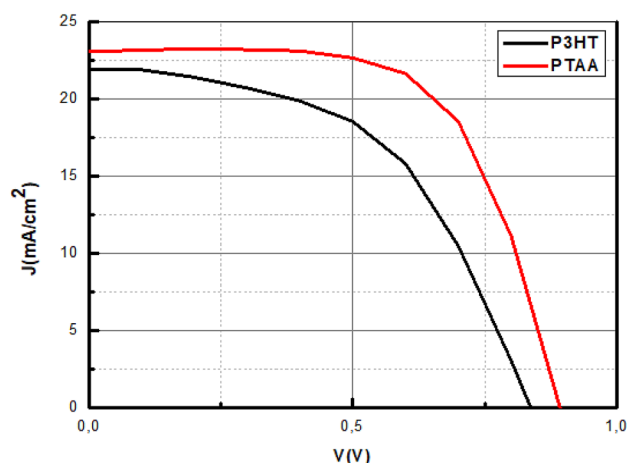


**Fig. 9** Current–voltage density characteristics of the best NIP cells under illumination for different HTL materials

### 3.2.3 Photovoltaic performance

In order to investigate the charge transport efficiency of the cells, J–V characteristics of the best PSCs with different HTL layers (P3HT versus PTAA) were investigated. The photocurrent–voltage (J–V) curves measured under simulated AM 1.5 sunlight conditions are shown in Fig. 9. The corresponding photovoltaic parameters are listed in Table 3. The high efficiency of 13.25% was obtained using the PTAA as HTL layer, with an open-circuit voltage ($V_{OC}$) of 0.89 V, a current density ($J_{SC}$) of 22.87 mA/cm$^2$, a fill factor (FF) of 64%, and a series resistance of 4.28 Ω.cm$^2$. The improvement of FF and $V_{OC}$ could be attributed to the enhancement of the perovskite film quality and low interface loss [47]. These results are in good agreement with the PL spectra and XRD measurements (Fig. 1 support information).

The performance parameters of the device based on CH$_3$NH$_3$PbI$_3$Cl$_x$/PTAA have also the highest $J_{SC}$ values than those of the device using P3HT. This increase of the short-circuit current is due to the elimination of the recombination pathways owing to an of perovskite film with good crystallinity [48].

Furthermore, in order to understand both enhanced $J_{SC}$ and FF, the series resistance ($R_S$) and the shunt resistance ($R_{Sh}$) are directly extracted from the J–V curve using the reverse of slope of J–V curve [49–51].

The PSCs based on PTAA have lower series resistances, while higher shunt resistance was obtained due to the reduced charge injection barrier between the perovskite and gold electrode [52].

### 3.3 Hysteresis effect

Figure 10 shows the J–V plots of the optimum standard cell with the structure: ITO/SnO$_2$/MAPbI$_{3-x}$Cl$_x$/PTAA/Au, in

**Table 3** Photovoltaic parameters extracted from the average solar cells fabricated from different HTL materials

| HTL material | | $V_{OC}$ (V) | $J_{SC}$ (mA/cm$^2$) | FF (%) | PCE (%) | $R_S$ (ohm.cm$^2$) | $R_{SC}$ (ohm.cm$^2$) |
|---|---|---|---|---|---|---|---|
| PTAA | Best | 0.89 | 22.87 | 64 | 13.3 | 4.28 | 596.67 |
| | Average | 0.85 | 20.37 | 61 | 10.7 | 7.73 | 839.57 |
| | Standard deviation | 24.58 | 2.46 | 7.96 | 0.22 | 3.73 | 667.47 |
| P3HT | Best | 0.83 | 21.32 | 57 | 10.1 | 5.59 | 276.07 |
| | Average | 0.92 | 21.64 | 59 | 11.7 | 10.51 | 309.37 |
| | Standard deviation | 22.60 | 1.32 | 0.32 | 0.94 | 2.4 | 827.93 |
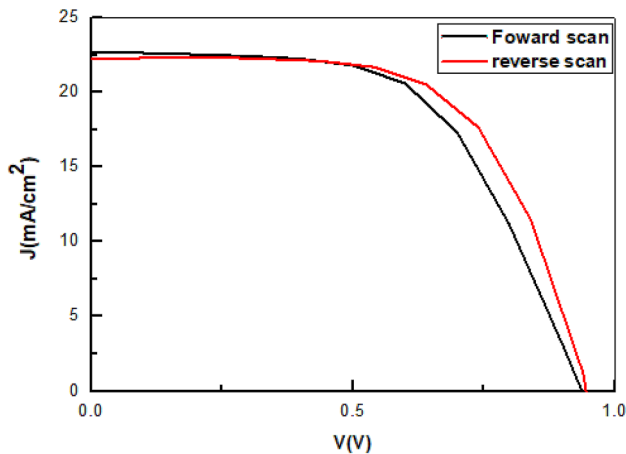


**Fig. 10** *J–V* plots of the best solar cell with forward and reverse scan

**Table 4** Photovoltaic performance of PSC based on MAPbI$_{3-x}$Cl$_{lx}$ with forward and reverse scan

| Device | $V_{OC}$ (V) | $J_{SC}$ (mA/cm$^2$) | FF (%) | PCE (%) |
|---|---|---|---|---|
| Forward scan | 0.89 | 22.87 | 64 | 13.3 |
| Reverse scan | 0.92 | 21.94 | 61 | 12.5 |

## 4 Conclusions

Due to outstanding material properties, organic–inorganic halide perovskites have attracted tremendous attention in the photovoltaic field. In this contribution, MAPbI$_{3-x}$Cl$_x$ perovskite solar cells using $SnO_2$ as an electron transport layer were elaborated. The effect of the annealing temperature of the $SnO_2$ layer was investigated. We reveal that the best annealing treatment of the $SnO_2$ is 220 °C, resulting in a highly efficient carrier's transportation with fewer defects at the interface SnO2/perovskite. We have also demonstrated that the performance of the device is also affected by the energy level of the HTL. The results show that the high PCE of the devices is obtained using the PTAA as an HTL, corresponding to the good charge transfer to HTL. With this approach, device efficiency could be raised from 10 to 13%.

## Compliance with ethical standards

**Conflicts of interest** There are no conflicts of interest to declare.

forward and reverse scan directions and the extracted parameters are summarized in Table 4. This cell achieves a PCE of 13.3% with a $V_{OC}$ of 0.89 V, a $J_{SC}$ of 22.87 mA/cm$^2$, and a FF of 64.57% under forwarding voltage scan. When the cell is measured in the reverse forward, a slight decrease in yield to 12.5% has been achieved with a $V_{OC}$ of 0.92 V, a $J_{SC}$ of 21.94 mA/cm$^2$, and an FF of 61.90%. A hysteresis behavior observed was the consequence of different physical effects. It can be probably due to the nature of the interfaces between the perovskite layer and the charge transport layers (ETL and HTL). Moreover, it can be attributed to ion accumulation [53, 54].

## References

1. A. Kojima, K. Teshima, Y. Shirai, T. Miyasaka, Organometal halide perovskites as visible-light sensitizers for photovoltaic cells. J. Am. Chem. Soc. **131**(17), 6050–6051 (2009)
2. H.S. Kim, C.R. Lee, J.H. Im, K.B. Lee, T. Moehl, A. Marchioro, M. Grätzel, Lead iodide perovskite sensitized all-solid-state submicron thin film mesoscopic solar cell with efficiency exceeding 9%. Sci. Rep. **2**, 591 (2012)
3. H. Zhou, Q. Chen, G. Li, S. Luo, T.B. Song, H.S. Duan, Y. Yang, Interface engineering of highly efficient perovskite solar cells. Science **345**(6196), 542–546 (2014)
4. W.S. Yang, J.H. Noh, N.J. Jeon, Y.C. Kim, S. Ryu, J. Seo, S.I. Seok, High performance photovoltaic perovskite layers fabricated through intramolecular exchange. Science **348**(6240), 1234–1237 (2015)

5. M. Saliba, T. Matsui, J.Y. Seo, K. Domanski, J.P. Correa-Baena, M.K. Nazeeruddin, M. Grätzel, Cesium-containing triple cation perovskite solar cells: improved stability, reproducibility and high efficiency. Energy Environ. Sci. **9**(6), 1989–1997 (2016)

6. https://www.nrel.gov/pv/cell-efficiency.html.

7. H.J. Snaith, Perovskites: the emergence of a new era for low-cost, high-efficiency solar cells. J. Phys. Chem. Lett. **4**(21), 3623–3630 (2013)

8. S. Gamliel, L. Etgar, Organo-metal perovskite based solar cells: sensitized versus planar architecture. RSC Adv. **4**(55), 29012–29021 (2014)

9. J.M. Ball, M.M. Lee, A. Hey, H.J. Snaith, Low-temperature processed meso superstructured to thin-film perovskite solar cells. Energy Environ. Sci. **6**(6), 1739–1743 (2013)

10. J.H. Im, C.R. Lee, J.W. Lee, S.W. Park, N.G. Park, 65% efficient perovskite quantum-dot-sensitized solar cell. Nanoscale **3**(10), 4088–4093 (2011)

11. N.G. Park, Organometal perovskite light absorbers toward a 20% efficiency low cost solid-state mesoscopic solar cell. J. Phys. Chem. Lett. **4**(15), 2423–2429 (2013)

12. S.D. Stranks, G.E. Eperon, G. Grancini, C. Menelaou, M.J. Alcocer, T. Leijtens, H.J. Snaith, Electron-hole diffusion lengths exceeding 1 micrometer in an organometal trihalide perovskite absorber. Science **342**(6156), 341–344 (2013)

13. G. Xing, N. Mathews, S. Sun, S.S. Lim, Y.M. Lam, M. Grätzel, T.C. Sum, Long-range balanced electron-and hole-transport lengths in organic-inorganic $CH_3NH_3PbI_3$. Science **342**(6156), 344–347 (2013)

14. H. Mehdi, A. Mhamdi, A. Bouazizi, Effect of perovskite precursor ratios and solvents volume on the efficiency of MAPbI3-xClx mixed halide perovskite solar cells. Mater. Sci. Semicond. Process. **109**, 104915 (2020)

15. L. Fan, Y. Ding, J. Luo, B. Shi, X. Yao, C. Wei, A. Hagfeldt, Elucidating the role of chlorine in perovskite solar cells. J. Mater. Chem. A **5**(16), 7423–7432 (2017)

16. J.H. Noh, S.H. Im, J.H. Heo, T.N. Mandal, S.I. Seok, Chemical management for colorful, efficient, and stable inorganic–organic hybrid nanostructured solar cells. Nano Lett. **13**(4), 1764–1769 (2013)

17. H. Mehdi, A. Mhamdi, R. Hannachi, A. Bouazizi, MAPbBr 3 perovskite solar cells via a two-step deposition process. RSC Adv. **9**(23), 12906–12912 (2019)

18. I.M. Dharmadasa, Y. Rahaq, A.A. Ojo, T.I. Alanazi, Perovskite solar cells: a deep analysis using current–voltage and capacitance. J. Mater. Sci. Mater. Electron. **30**(2), 1227–1235 (2019)

19. W. Kim, J. Park, H. Kim, Y. Pak, H. Lee, G.Y. Jung, Sequential dip-spin coating method: fully infiltration of MAPbI3-xClx into mesoporous TiO2 for stable hybrid perovskite solar cells. Electrochim. Acta **245**, 734–741 (2017)

20. Y. Li, X. Qi, W. Wang, C. Gao, N. Zhu, G. Liu, Y. Zhang, F. Lv, B. Qu, Planar inverted perovskite solar cells based on the electron transport layer of PC61BM: ITIC. Synth. Met. **245**, 116–120 (2018)

21. H. Mehdi, A. Mhamdi, A. Bouazizi, Effect of annealing treatment on the properties of inverted solar cells based on mixed halide perovskite. Physica E **119**, 114000 (2020)

22. A. Dubey, N. Adhikari, S. Mabrouk, F. Wu, K. Chen, S. Yang, Q. Qiao, Astrategic review on processing routes towards highly efficient perovskite solar cells. J. Mater. Chem. A **6**(6), 2406–2431 (2018)

23. M. Saliba, T. Matsui, K. Domanski, J.Y. Seo, A. Ummadisingu, S.M. Zakeeruddin, J.P. Correa-Baena, W.R. Tress, A. Abate, A. Hagfeldt, M. Grätzel, Incorporation of rubidium cations into perovskite solar cells improves photovoltaic performance. Science **354**(6309), 206–209 (2016)

24. W. Rehman, D.P. McMeekin, J.B. Patel, R.L. Milot, M.B. Johnston, H.J. Snaith, L.M. Herz, Photovoltaic mixed-cation lead mixed-halide perovskites: links between crystallinity, photostability and electronic properties. Energy Environ. Sci. **10**(1), 361–369 (2017)

25. Y.H. Seo, E.C. Kim, S.P. Cho, S.S. Kim, S.I. Na, High-performance planar perovskite solar cells: Influence of solvent upon performance. Appl. Mater. Today **9**, 598–604 (2017)

26. J. Zhang, F. Li, K. Yang, C.P. Veeramalai, T. Guo, Low temperature processed planar heterojunction perovskite solar cells employing silver nanowires as top electrode. Appl. Surf. Sci. **369**, 308–313 (2016)

27. G. Wang, J. Liu, K. Chen, R. Pathak, A. Gurung, Q. Qiao, High-performance carbon electrode-based CsPbI2Br inorganic perovskite solar cell based on poly (3-hexylthiophene)-carbon nanotubes composite hole-transporting layer. J. Colloid Interface Sci. **555**, 180–186 (2019)

28. M.S. Chowdhury, S.A. Shahahmadi, P. Chelvanathan, S.K. Tiong, N. Amin, K. Techato, N. Nuthammachot, T. Chowdhury, M. Suklueng, Effect of deep-level defect density of the absorber layer and n/i interface in perovskite solar cells by SCAPS-1D. Results Phys. **16**, 102839 (2020)

29. D. Liu, S. Li, P. Zhang, Y. Wang, R. Zhang, H. Sarvari, F. Wang, J. Wu, Z. Wang, Z.D. Chen, Efficient planar heterojunction perovskite solar cells with Li-doped compact $TiO_2$ layer. Nano Energy **31**, 462–468 (2017)

30. A. Mhamdi, H. Mehdi, A. Bouazizi, G. Garcia-Belmonte, One-step methylammonium lead bromide films: effect of annealing treatment. J. Mol. Struct. **1192**, 1–6 (2019)

31. Z. Zhu, X. Zheng, Y. Bai, T. Zhang, Z. Wang, S. Xiao, S. Yang, Mesoporous $SnO_2$ single crystals as an effective electron collector for perovskite solar cells. Phys. Chem. Chem. Phys. **17**(28), 18265–18268 (2015)

32. L. Zuo, Z. Gu, T. Ye, W. Fu, G. Wu, H. Li, H. Chen, Enhanced photovoltaic performance of CH3NH3PbI3 perovskite solar cells through interfacial engineering using self assembling monolayer. J. Am. Chem. Soc. **137**(7), 2674–2679 (2015)

33. J. Geng, B.S. Kong, S.B. Yang, S.C. Youn, S. Park, T. Joo, H.T. Jung, Effect of SWNT defects on the electron transfer properties in P3HT/SWNT hybrid materials. Adv. Func. Mater. **18**(18), 2659–2665 (2008)

34. J.C. Ke, Y.H. Wang, K.L. Chen, C.J. Huang, Effect of temperature annealing treatments and acceptors in $CH_3NH_3PbI_3$ perovskite solar cell fabrication. J. Alloy. Compd. **695**, 2453–2457 (2017)

35. T.Y. Chiang, G.L. Fan, J.Y. Jeng, K.C. Chen, P. Chen, T.C. Wen, K.T. Wong, Functional p-type, polymerized organic electrode interlayer in $CH_3NH_3PbI_3$ perovskite/fullerene planar heterojunction hybrid solar cells. ACS Appl. Mater. Interfaces. **7**(44), 24973–24981 (2015)

36. M. Jiang, J. Wu, F. Lan, Q. Tao, D. Gao, G. Li, Enhancing the performance of planar organo-lead halide perovskite solar cells by using a mixed halide source. J. Mater. Chem. A **3**(3), 963–967 (2015)

37. C. Huang, N. Fu, F. Liu, L. Jiang, X. Hao, H. Huang, Highly efficient perovskite solar cells with precursor composition-dependent morphology. Sol. Energy Mater. Sol. Cells **145**, 231–237 (2016)

38. M. Liu, M.B. Johnston, H.J. Snaith, Efficient planar heterojunction perovskite solar cells by vapour deposition. Nature **501**(7467), 395 (2013)

39. T. Baikie, N.S. Barrow, Y. Fang, P.J. Keenan, P.R. Slater, R.O. Piltz, T.J. White, A combined single crystal neutron/X-ray diffraction and solid-state nuclear magnetic resonance study of the hybrid perovskites $CH_3NH_3PbX_3$ (X= I, Br and Cl). J. Mater. Chem. A **3**(17), 9298–9307 (2015)

40. C. Sun, Y. Guo, B. Fang, L. Guan, H. Duan, Y. Chen, H. Liu, Facile preparation of high-quality perovskites for efficient solar cells via a fast conversion of wet PbI$_2$ precursor films. RSC Adv. **7**(36), 22492–22500 (2017)

41. Y. Liu et al., Fabrication and photovoltaic performance of niobium doped TiO$_2$ hierarchical microspheres with exposed 001 facets and high specific surface area. Appl. Surf. Sci. **410**, 241–248 (2017)

42. T.J. Jacobsson, J.P. Correa-Baena, E. HalvaniAnaraki, B. Philippe, S.D. Stranks, M.E. Bouduban, H. Rensmo, Unreacted PbI$_2$ as a double-edged sword for enhancing the performance of perovskite solar cells. J. Am. Chem. Soc. **138**(32), 10331–10343 (2016)

43. B.W. Park, B. Philippe, T. Gustafsson, K. Sveinbjörnsson, A. Hagfeldt, E.M. Johansson, G. Boschloo, Enhanced crystallinity in organic–inorganic lead halide perovskites on mesoporous TiO2 via disorder–order phase transition. Chem. Mater. **26**(15), 4466–4471 (2014)

44. X. Cao, L. Zhi, Y. Jia, Y. Li, K. Zhao, X. Cui, J. Wei, Enhanced efficiency of perovskite solar cells by introducing controlled chloride incorporation into MAPbI$_3$ perovskite films. Electrochim. Acta **275**, 1–7 (2018)

45. Z. Zhu, Y. Bai, X. Liu, C.C. Chueh, S. Yang, A.K.Y. Jen, Enhanced efficiency and stability of inverted perovskite solar cells using highly crystalline SnO2 nanocrystals as the robust electron-transporting layer. Adv. Mater. **28**(30), 6478–6484 (2016)

46. S. Juillard, Optimisation des interfaces de systèmes PV organiques encapsulés. Doctoral dissertation, Grenoble Alpes, 2018.

47. S. Jin, Y. Wei, F. Huang, X. Yang, D. Luo, Y. Fang, J. Wu, Enhancing the perovskite solar cell performance by the treatment with mixed anti-solvent. J. Power Sour. **404**, 64–72 (2018)

48. H.B. Kim, I. Im, Y. Yoon, S. Do Sung, E. Kim, J. Kim, W.I. Lee, Enhancement of photovoltaic properties of CH$_3$NH$_3$PbBr$_3$ heterojunction solar cells by modifying mesoporous TiO$_2$ surfaces with carboxyl groups. J. Mater. Chem. A **3**(17), 9264–9270 (2015)

49. F. Xia, Q. Wu, P. Zhou, Y. Li, X. Chen, Q. Liu, J. Zhu, S. Dai, Y. Lu, S. Yang, Efficiency enhancement of inverted structure perovskite solar cells via oleamide doping of PCBM electron transport layer. ACS Appl. Mater. Interfaces **7**(24), 13659–13665 (2015)

50. S. Mabrouk, M. Zhang, Z. Wang, M. Liang, B. Bahrami, Y. Wu, J. Wu, Q. Qiao, S. Yang, Dithieno [3, 2-b: 2′, 3′-d] pyrrole-based hole transport materials for perovskite solar cells with efficiencies over 18%. J. Mater. Chem. A **6**(17), 7950–7958 (2018)

51. X. Huang, K. Wang, C. Yi, T. Meng, X. Gong, Efficient perovskite hybrid solar cells by highly electrical conductive PEDOT: PSS hole transport layer. Adv. Energy Mater. **6**(3), 1501773 (2016)

52. P. Chen, E. Wang, X. Yin, H. Xie, M. Que, B. Gao, W. Que, Additive-assisted one-step formed perovskite/hole conducting materials graded heterojunction for efficient perovskite solar cells. J. Colloid Interface Sci. **532**, 182–189 (2018)

53. F. Wu, R. Pathak, K. Chen, G. Wang, B. Bahrami, W.H. Zhang, Q. Qiao, Invertedcurrent–voltage hysteresis in perovskitesolarcells. ACS Energy Lett. **3**(10), 2457–2460 (2018)

54. F. Wu, B. Bahrami, K. Chen, S. Mabrouk, R. Pathak, Y. Tong, X. Li, T. Zhang, R. Jian, Q. Qiao, Bias-dependent normal and inverted J-V hysteresis in perovskitesolarcells. ACS Appl. Mater. Interfaces **10**(30), 25604–25613 (2018)